

## The star formation history of redshift $z \sim 2$ galaxies: the role of the infrared prior \*

Lu-Lu Fan<sup>1,2,3</sup>, Andrea Lapi<sup>4,3</sup>, Alessandro Bressan<sup>3</sup>, Mario Nonino<sup>5</sup>,  
Gianfranco De Zotti<sup>3</sup> and Luigi Danese<sup>3</sup>

<sup>1</sup> Center for Astrophysics, University of Science and Technology of China, Hefei 230026, China; [llfan@ustc.edu.cn](mailto:llfan@ustc.edu.cn)

<sup>2</sup> Key Laboratory for Research in Galaxies and Cosmology, Chinese Academy of Sciences, Hefei 230026, China

<sup>3</sup> Astrophysics Sector, SISSA, Via Bonomea 265, 34136 Trieste, Italy

<sup>4</sup> Dip. Fisica, Univ. ‘Tor Vergata’, Via Ricerca Scientifica 1, 00133 Roma, Italy

<sup>5</sup> INAF-Osservatorio Astronomico di Trieste, Via G.B. Tiepolo 11, 40131 Trieste, Italy

Received 2013 May 3; accepted 2013 August 30

**Abstract** We build a sample of 298 spectroscopically-confirmed galaxies at redshift  $z \sim 2$ , selected in the  $z_{850}$ -band from the GOODS-MUSIC catalog. By utilizing the rest frame  $8 \mu\text{m}$  luminosity as a proxy of the star formation rate (SFR), we check the accuracy of the standard SED-fitting technique, finding it is not accurate enough to provide reliable estimates of the physical parameters of galaxies. We then develop a new SED-fitting method that includes the IR luminosity as a prior and a generalized Calzetti law with a variable  $R_V$ . Then we exploit the new method to re-analyze our galaxy sample, and to robustly determine SFRs, stellar masses and ages. We find that there is a general trend of increasing attenuation with the SFR. Moreover, we find that the SFRs range between a few to  $10^3 M_\odot \text{yr}^{-1}$ , the masses from  $10^9$  to  $4 \times 10^{11} M_\odot$ , and the ages from a few tens of Myr to more than 1 Gyr. We discuss how individual age measurements of highly attenuated objects indicate that dust must have formed within a few tens of Myr and already been copious at  $\leq 100$  Myr. In addition, we find that low luminosity galaxies harbor, on average, significantly older stellar populations and are also less massive than brighter ones; we discuss how these findings and the well known ‘downsizing’ scenario are consistent in a framework where less massive galaxies form first, but their star formation lasts longer. Finally, we find that the near-IR attenuation is not scarce for luminous objects, contrary to what is customarily assumed; we discuss how this affects the interpretation of the observed  $M_*/L$  ratios.

**Key words:** cosmology: observations — galaxies: evolution — galaxies: high redshift — galaxies: stellar content — dust, extinction

---

\* Supported by the National Natural Science Foundation of China.

## 1 INTRODUCTION

Dust plays a crucial role in the formation and evolution of galaxies. It absorbs stellar light and re-emits in the far infrared (FIR). Even a small amount of dust can lead to a significant underestimation of the star formation rate (SFR). Poggianti & Wu (2000), Poggianti et al. (2001) and Rigopoulou et al. (2000) reported independent evidence on both local and high-redshift luminous starbursts in which  $\sim 70\%$ – $80\%$  of the bolometric flux from young stars is completely obscured by dust and remains hidden in the  $UV$ /optical surveys (even after correction for dust).

Dust constitutes a fundamental physical component in active star-forming galaxies. In fact, the dust formation is closely related to the star formation activity, as it occurs in a range of environments, from explosive ejecta of supernovae to the outflows of evolved low-mass stars (Dwek 1998). Moreover, the presence of dust can enhance the SFR (Hirashita & Ferrara 2002; Morgan & Edmunds 2003), as the surface of dust grains constitutes a site for efficient formation of  $H_2$  molecules (e.g. Cazaux & Tielens 2002, 2004), which act as an effective coolant in metal-poor interstellar media. In fact, such a correlation has been found in both low and high redshift galaxies (Adelberger & Steidel 2000; Vijh et al. 2003; Ouchi et al. 2004; Shapley et al. 2001, 2005).

To represent dust attenuation, most authors use the  $UV$  slope  $\beta_{UV}$ , and adopt the Meurer relation as derived from a sample of local starburst galaxies (Meurer et al. 1999); other authors instead use the color excess  $E(B - V)$  as inferred from the spectral energy distribution (SED) of galaxies, and adopt a Calzetti extinction law similar to the Meurer relation (Calzetti et al. 2000). However, not only is the validity of the local Meurer relation at high redshift currently under debate, but even in local normal star-forming galaxies (i.e. Bell 2002; Seibert et al. 2005; Boissier et al. 2007; Buat et al. 2005; Burgarella et al. 2005; Gil de Paz et al. 2007; Cortese et al. 2006) and individual HII regions (Calzetti et al. 2005), there are clear deviations from it. The most useful indicator of dust obscuration should be infrared to ultraviolet luminosity ratio (IRX), which is relatively independent of star formation history (Buat et al. 2005) and of the dust configuration and distribution (Witt & Gordon 2000).

Unfortunately, it is difficult to directly trace the infrared luminosity of typical star forming galaxies at high redshift by their far-infrared or submillimeter emission, due to the current sensitivity limits of bolometers and submillimeter interferometers. We must look for other portions of the SED to examine dust emissions. A possible way is to use the mid-infrared (mid-IR) dust emission of galaxies as a tracer of total infrared luminosity. The correlation between mid-IR and infrared luminosity has been revealed in both the local and  $z \sim 1$  Universe with the observations of the *Infrared Space Observatory* (Boselli et al. 1998; Adelberger & Steidel 2000; Dale et al. 2000; Helou et al. 2000; Förster Schreiber et al. 2003) and the Spitzer MIPS (Rieke et al. 2009). This relation has been also examined at  $z \sim 2$  by X-ray and radio stacking analysis (Reddy et al. 2006) and Spitzer MIPS 24  $\mu\text{m}$  observations (Reddy et al. 2010). Taking the IRX derived from rest-frame 8  $\mu\text{m}$  luminosity  $L_8$  as a reference, one can test to what extent the  $UV$  slope  $\beta_{UV}$  is an effective probe of dust attenuation.

Another fundamental physical measurement for high redshift galaxies is constituted by the stellar mass. Stellar population synthesis modeling is popularly used to estimate stellar mass at high redshift (e.g. Sawicki & Yee 1998; Papovich et al. 2001, 2004, 2006; Shapley et al. 2005; Förster Schreiber et al. 2004). In particular, a number of authors in recent years have interpreted observed-frame  $UV$  to near-IR (even mid-IR) photometry with stellar population synthesis models in order to infer stellar masses and the total mass as a function of redshift (e.g. Papovich et al. 2001; Shapley et al. 2001, 2005; Daddi et al. 2004; Dickinson et al. 2003; Fontana et al. 2003; Labbé et al. 2005; Pérez-González et al. 2008). At  $z \sim 2$ ,  $H\alpha$ + $[NII]$  line emissions will be moved into the  $K_S$  band, and one has to take the nebular spectrum into account in order to obtain precise evaluations of stellar masses. We stress that, although Papovich et al. (2001) have tested the impact of different metallicities, initial mass functions (IMFs) and star formation histories on determinations of stellar mass, the effects of assumptions concerning the dust extinction law have to be checked in detail.

In this paper, we investigate dust attenuations, star formation histories and stellar masses in  $z \sim 2$  galaxies. For this purpose, we exploit a data set spanning the electromagnetic spectrum from  $UV$  to mid-IR, supplemented by Spitzer MIPS 24  $\mu\text{m}$  photometry and spectroscopic redshift determinations. We aim to show that, in order to robustly evaluate the star formation history and stellar mass at high redshift, the rest-frame SEDs from  $UV$  to near-IR must be complemented by the IR luminosity, or at least by a robust prior for it.

The plan of the paper is as follows: in Section 2 we describe our sample selection; in Section 3 we discuss the relation between the rest-frame  $UV$  slope and dust attenuation; in Section 4 and in the Appendix we give details on our stellar population synthesis model; in Section 5 we present our results; in Section 6 we summarize our main conclusions. Throughout the paper we assume a concordance  $\Lambda\text{CDM}$  cosmology with  $\Omega_m = 0.27$ ,  $\Omega_\Lambda = 0.73$  and  $h = 0.71$ .

## 2 THE SAMPLE SELECTION

The data are taken directly from the Version 2 release of the GOODS MULTicolor Southern Infrared Catalog (GOODS-MUSIC) sample (Santini et al. 2009). The main differences between Version 1 (Grazian et al. 2006) and Version 2 of the GOODS-MUSIC sample are basically the following three points: (1) the IRAC photometry is improved using new IRAC PSFs and background subtraction for the 3.6, 4.5, 5.8 and 8.0  $\mu\text{m}$  bands; (2) new spectroscopic redshifts are added that became available after the Version 1 release; (3) the 24  $\mu\text{m}$  photometry by the MIPS instrument are added.

We start our work from the  $z_{850}$ -selected catalog which has a typical  $z_{850}$ -band magnitude limit,  $z_{850} = 26.0$ , for most of the catalog and extends down to  $z_{850} = 26.18$  in limited areas. The galaxies are selected from the  $z_{850}$ -selected catalog with the flag `selgal = 1`. Thanks to the releases of new spectra in the GOODS-South Field (FORS2: Vanzella et al. 2006, 2008; VIMOS: Popesso et al. 2009, Balestra et al. 2010), we can use a much larger spectroscopic sample than that presented in Grazian et al. (2006). The quality of all spectroscopic redshifts is marked with a `quality_flag` flag which is divided into four classes: very good, good, uncertain and very uncertain, represented by 0, 1, 2 and 3, respectively. We discard those galaxies with uncertain spectroscopic redshifts (`quality_flag = 2` or 3).

The photometric measurements used to model the stellar populations are comprised of 12 bands, namely the  $U$ -band from the 2.2ESO ( $U_{35}$  and  $U_{38}$ ) and VLT-VIMOS ( $U_{\text{VIMOS}}$ ), the  $F435W$  ( $B$ -band),  $F606W$  ( $V$ -band),  $F775W$  ( $i$ -band), and  $F850LP$  ( $z_{850}$ -band) HST/ACS data, the  $JHK_S$  VLT data, and the 3.6, 4.5, 5.8 and 8.0  $\mu\text{m}$  bands from the Spitzer IRAC instrument. We use  $U_{\text{VIMOS}}$  instead of  $U_{35}$  and  $U_{38}$  because the former is much deeper than the other two. We only select galaxies with at least one  $JHK_S$  band, at least one of four IRAC bands and at least seven bands detected in total.

In this way we get a spectroscopic sample of 298  $z_{850}$ -selected galaxies within the redshift range  $1.4 \leq z \leq 3.0$ . We notice that most of our low redshift galaxies at  $z \leq 1.7$  are taken from FORS2 spectra which have red  $i - z_{850}$  colors ( $i - z_{850} = 0.35 \pm 0.21$  in our sample). Most of our high redshift galaxies at  $z \geq 1.7$  are taken from VIMOS spectra which have blue  $i - z_{850}$  colors ( $i - z_{850} = 0.09 \pm 0.17$  in our sample). Finally, public 24  $\mu\text{m}$  Spitzer MIPS observations have also been exploited. A PSF-matching technique, which is performed by the software `ConvPhot` (de Santis et al. 2007), has been employed to properly detect and deblend objects in the MIPS images (Santini et al. 2009). As a result, 135 out of 298 galaxies are also detected in the 24  $\mu\text{m}$  band. We emphasize that galaxies in the  $z_{850}$ -selected sample at  $z \sim 2$  are expected to be star forming as the sample is basically selected from the rest-frame  $UV$  band. A diagnostic BzK diagram confirms this idea: over 95% galaxies are sBzk.

The existence of a tight correlation between the rest-frame 8  $\mu\text{m}$  luminosity  $\mu L_\mu$  (hereafter  $L_8$ ) and the 8 – 1000  $\mu\text{m}$  IR luminosity (hereafter  $L_{\text{IR}}$ ), initially established for local star forming galaxies, has been confirmed for large samples of galaxies in a wide range of luminosity and redshift,

thanks to the advent of the Herschel satellite (see Chary & Elbaz 2001; Caputi et al. 2007; Dale et al. 2000; Bavouzet et al. 2008; Rieke et al. 2009; Elbaz et al. 2011; Nordon et al. 2010, 2012; Reddy et al. 2010, 2012a). Although the dependence on redshift and luminosity is very weak, it has been suggested that the most relevant parameter involved in shaping the above relationship is the projected star formation density, as inferred from the IR surface brightness (Elbaz et al. 2011; Nordon et al. 2012; Reddy et al. 2012a). While extended galaxies exhibit a median ratio  $\text{IR8} = L_{\text{IR}}/L_8 \approx 5$ , the median IR8 of the compact objects is larger by a factor of around 2. These altogether exhibit a median  $\text{IR8} \approx 8.5$ , in agreement with the finding of Rigby et al. (2008) for a sample of lensed galaxies at  $z \sim 2$ . In the following, we will assume the median value  $\text{IR8} = 8.5$  as a reference for our sample, in order to estimate the IR luminosity from  $24 \mu\text{m}$  observations. Following Elbaz et al. (2011) this value will possibly overestimate the inferred  $L_{\text{IR}}$  of normal star-forming galaxies while it will underestimate that of compact starbursts.

Since the median redshift of our sample is  $z \sim 2$ , galaxies are typically selected in the rest-frame  $U$  band with broadband spectra from  $1200 \text{ \AA}$  to the near-IR. Moreover, for the objects detected at  $8 \mu\text{m}$  we can use the IR8 relation to estimate the IR luminosity. We notice that at those redshifts a direct measure of the IR luminosity is only achievable (e.g., with Herschel) for  $\text{SFR} \geq 10^2 M_{\odot} \text{ yr}^{-1}$ . On the other hand, with our current selection we can reach  $\text{SFR} \geq 10 M_{\odot} \text{ yr}^{-1}$ . Thus our selection allows us to perform a detailed study of the properties of galaxies over a wide range of parameters, such as stellar mass, age, SFR and dust content.

### 3 THE $\text{IRX}-\beta_{UV}$ RELATION AT HIGH REDSHIFT

We have selected a sample of high redshift galaxies for which the whole rest-frame SED from  $UV$  to near-IR is available, together with a robust proxy of the IR luminosity, i.e., the amount of light absorbed by dust. The latter quantity could be directly used together with the observed  $UV$  luminosity to derive the bolometric luminosity and hence the ongoing SFR of the galaxy. However, in order to obtain other relevant physical parameters such as the age and the mass of the galaxy, we need to utilize the technique of population synthesis. This requires a few additional approximations concerning the dust attenuation, the star formation law, the initial mass function and the metallicity of the stellar populations.

A detailed description of dust attenuation would require analyzing the chemical composition and size of dust grains, the spatial distribution of dust and stars in the galaxy and the solutions of the radiative transfer equation (see ; Dwek 1998; Silva et al. 1998; Draine 2003, and many others). However, many observational results can be rendered and understood by treating the galaxy as a point-like source behind a screen of dust (see Calzetti et al. 1994; Meurer et al. 1999).

To get insight on the form of the attenuation law, the observed  $UV$  data and the IR luminosity can be combined to construct the so called  $\text{IRX}-\beta_{UV}$  diagram; we recall that  $\text{IRX}$  is the IR to  $UV$  luminosity ratio and  $\beta_{UV}$  is the rest-frame  $UV$  slope. In spite of the fact that both quantities are expected to be strongly affected by the strength and by the wavelength dependence of the attenuation law, Meurer et al. (1999) have pointed out the existence of a tight  $\text{IRX}-\beta_{UV}$  correlation in local starburst galaxies, indicating a quite universal form of the attenuation law. Such correlation has been found to hold even in high redshift  $z \sim 2$  samples (Reddy et al. 2006, 2010; Elbaz et al. 2011), though with a larger scatter.

For our sample, we have computed the  $UV$  slope by performing a linear fit to all available photometric data with rest-frame central wavelengths falling in the range  $1250 - 2600 \text{ \AA}$ . The observed  $L_{UV}$  is approximated by the quantity  $L_{1600} = \lambda(1600)L_{\lambda}(1600)$ , while the *observed* IR luminosity  $L_{\text{IR}}$  is derived by the  $8 \mu\text{m}$  rest-frame luminosity by assuming the ratio  $\text{IR8} = 8.5$  as discussed in Section 2.

The results are shown in Figure 1 where galaxies are depicted with different colors, following their IR luminosities; in particular, galaxies with  $L_{\text{IR}} > 10^{12} L_{\odot}$  (ultraluminous infrared galaxies,

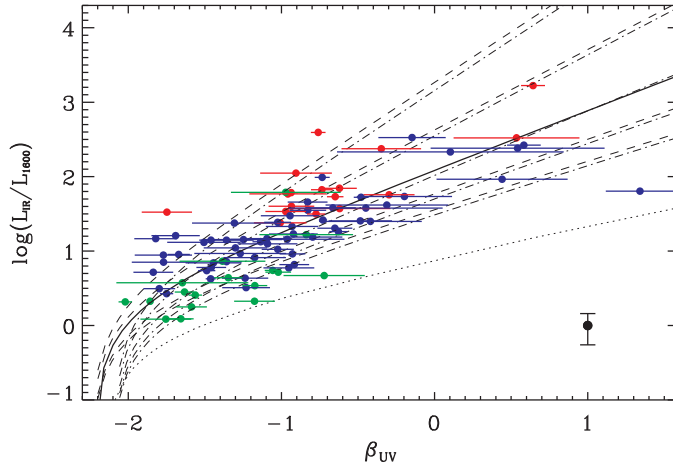


**Fig. 1** The rest-frame IRX- $\beta_{UV}$  relation for our sample. Data points are color-coded according to their IR luminosity, which is obtained from the rest-frame 8  $\mu\text{m}$  luminosity by adopting a ratio  $\text{IR}8 = 8.5$ , see Section 2 for details. Specifically, red points refer to  $L_{\text{IR}} > 10^{12} L_{\odot}$ , blue to  $10^{11} L_{\odot} \leq L_{\text{IR}} \leq 10^{12} L_{\odot}$  and green to  $L_{\text{IR}} < 10^{11} L_{\odot}$ . The solid line shows the local Meurer relation, while the dotted line shows the corresponding relation obtained on adopting the SMC extinction law. The dashed lines are our models with solar metallicity,  $100 M_{\odot} \text{yr}^{-1}$  constant SFR, and age of 0.1 Gyr for an increasing value of the  $R_V$  parameter in the Calzetti law (see Eq. (1)), from  $R_V = 1.5$  (bottom dashed curve) to  $R_V = 10$  (top dashed curve). Along the curves,  $E(B - V)$  increases from 0 to a suitable upper limit. The dot-dashed lines represent the same but with an older average age of 1 Gyr.

ULIRGs) are in red, those with  $10^{11} L_{\odot} \leq L_{\text{IR}} \leq 10^{12} L_{\odot}$  (luminous infrared galaxies, LIRGs) are in blue, and those with  $L_{\text{IR}} < 10^{11} L_{\odot}$  (lower luminosity infrared galaxies, LLIRGs) are in green. The solid line represents a model of solar metallicity and a constant SFR =  $100 M_{\odot} \text{yr}^{-1}$  with age of 0.1 Gyr.  $E(B - V)$  increases along the curve, starting from 0 at the bottom left. We have adopted the Calzetti law (cf. eqs. (3) and (4) in Calzetti et al. 2000)

$$A(\lambda) = E(B - V)(f_{\lambda} + R_V) \quad (1)$$

with  $f_{\lambda} = 2.659 \times (-1.857 + 1.040/\lambda)$  for  $0.63 \mu\text{m} \leq \lambda \leq 2.20 \mu\text{m}$  and  $f_{\lambda} = 2.659 \times (-2.156 + 1.509/\lambda - 0.198/\lambda^2 + 0.011/\lambda^3)$  for  $0.12 \mu\text{m} \leq \lambda \leq 0.63 \mu\text{m}$  and  $R_V = 4.05$ .

The observed luminosity of the model is given by

$$L_{\text{obs}}(\lambda) = L_{\text{int}}(\lambda)10^{-0.4A(\lambda)}, \quad (2)$$

where  $L_{\text{int}}(\lambda)$  is the intrinsic stellar luminosity. The IR luminosity of the model can be derived from

$$L_{\text{IR}} \approx L_{\text{abs}} = \int_0^{\infty} L_{\text{int}}(\lambda)[1 - 10^{-0.4A(\lambda)}]d\lambda, \quad (3)$$

where  $L_{\text{abs}}$  is the absorbed luminosity. We recall that the Calzetti law reproduces the Meurer relation for local starbursts fairly well.

From Figure 1 it is seen that on average our galaxies follow a trend that is consistent with other recent studies at  $z \sim 2$  (Reddy et al. 2006, 2010; Elbaz et al. 2011). However, the individual observations show a large scatter. In particular, the Meurer relation seems to be the lower envelope

for the more luminous galaxies with  $L_{\text{IR}} > 10^{12} L_{\odot}$  and the upper envelope for the less luminous ones with  $L_{\text{IR}} < 10^{11} L_{\odot}$ . The scatter is larger than that allowed by the uncertainty in the estimate of IR luminosity through the IR8 ratio. Indeed, systematically larger IRX ratios are also found in the local ULIRGs (Goldader et al. 2002), in  $z \sim 2$  ULIRGs (Reddy et al. 2010) and in radio-selected submillimeter bright galaxies (Chapman et al. 2005). This bias is generally attributed to the fact that a significant fraction of the star formation is strongly obscured at the  $UV$  band. The observed  $UV$  photons are not responsible for most of the IR luminosity; rather they are formed earlier and have already escaped from dusty environments (Silva et al. 1998; Reddy et al. 2006; Papovich et al. 2006; Chapman et al. 2005). On the other hand, values of the IRX ratios lower than what is predicted by the Meurer relation are generally ascribed to different extinction laws. An example is that of the Small Magellanic Cloud (SMC), which is represented by the dotted line (e.g. Pettini et al. 1998).

A few important points can be inferred from examining Figure 1. First of all, the scatter of the data points shows that the SFR cannot be robustly predicted on the basis of the  $UV$  SED alone. This highlights once more the importance of having a robust estimator of the total IR luminosity. Second, we infer that it is impossible to simultaneously fit the IR data on one side and the  $UV$  SED on the other, if one assumes a single form (not strength) of the attenuation law (even by letting the age change within the values allowed by their observed redshift, see below). To better clarify this point we have plotted the results of other attenuation curves in the same figure (dashed lines). They have been obtained from the solid curve by varying the parameter  $R_V$  from the Calzetti value 4.05. It is seen that the data can be fairly well reproduced if we let  $R_V$  change in the interval from 1.5 (bottom dashed curve) to 10 (top dashed curve). Increasing the parameter  $R_V$  flattens the attenuation law, as can be immediately seen by casting Equation (1) in the following form

$$A(\lambda)/A(V) = f_{\lambda}/R_V + 1. \quad (4)$$

Such variation of the parameter  $R_V$  is meant not only to render the effects of different properties of the dust on the *extinction*, but also to describe at first-order other complex effects such as variations of the dust/star geometry.

Effects of age are also important, but only at low values of  $\beta_{UV} \leq -2$  where the IRX- $\beta_{UV}$  diagram becomes insensitive to  $R_V$  because the attenuation is also small. On the other hand, at high  $\beta_{UV} \geq -2$  age effects are negligible, as illustrated by the dot-dashed lines that represent the same models as above but with an older average age (1 Gyr instead of 0.1 Gyr).

#### 4 STELLAR POPULATION SYNTHESIS MODELING

In light of the above discussion, now we turn to the issue of performing a robust estimation of the galaxy parameters via the SED fitting technique. Our procedure consists of simultaneously modeling both the detailed rest frame SED, from the far  $UV$  to the near-IR, and the total luminosity absorbed by dust as predicted from the observed  $24 \mu\text{m}$  flux. For this purpose we use a set of simple stellar populations (SSPs) with solar metallicity and a Chabrier (2003) IMF extending from 0.15 to  $120 M_{\odot}$ . The adopted SSPs are described in more detail in Appendix A.

As shown by Shapley et al. (2004, 2005), solar metallicity is a good approximation in  $z \geq 2$  galaxies. In any case, we have checked that varying the chemical composition from solar to 1/3 solar does not significantly change our results. In fact, for younger stellar populations the effect of metallicity is less severe than for older ones, as found in the local Universe. Different kinds of IMFs such as Salpeter (1955) or Kroupa (2001), and different stellar mass ranges for them will change the final stellar mass up to a factor  $\leq 1.6$ .

For the sake of simplicity, in this paper we have considered the case of constant SFR. Other parameterizations are also often used in the literature, involving an exponential increase, exponential decrease or a sequence of both. In sophisticated galaxy formation models (e.g., Granato et al. 2004; Fan et al. 2008, 2010; Lapi et al. 2006, 2011), the SFR initially increases, attains an approximately

constant value, and then is quenched by the energetic feedback from supernovae or quasars (soon after one Gyr for strongly star-forming sources, and after several Gyrs for weakly star-forming ones). Then the constant SFR adopted here is a fairly good representation of the average behavior expected for these objects during most of the time they spend as star-forming sources. This is also in agreement with the recent analysis by Reddy et al. (2012b) of a large spectroscopic galaxy sample at redshift  $1.4 \leq z \leq 3.7$  based on *Hubble* and *Spitzer* observations.

We include the total IR luminosity in the calculation, and treat the predicted value as a constraint in the SED-fitting minimization procedure. The predicted IR luminosity is computed using Equation (3), while the observed IR luminosity is derived from the 24  $\mu\text{m}$  flux as described in Section 2. The attenuation law is assumed to be independent of age and parameterized by means of Equation (1). However, according to the previous discussion on the  $\text{IRX}-\beta_{UV}$  relation in Section 3, the  $R_V$  value in Equation (1) is considered as a free parameter in the fitting procedure (see also the discussion in Calzetti et al. 2000). It was allowed to vary in the range 1.5 – 10, which as discussed before provides a fair representation of the dispersion in Figure 1.

The model contains four parameters: the strength of the constant SFR, the age of the galaxy  $t_g$  (limited only by the consistency with the observed redshift), the strength of the attenuation parameterized by  $E(B - V)$  and the parameter  $R_V$ . Then we compute the intrinsic spectrum of the galaxy, to which we apply the internal reddening. The absorbed spectrum is integrated to provide the model IR luminosity which is constrained by the corresponding observed quantity. Finally, after applying the attenuation due to the intervening intergalactic neutral hydrogen (Madau 1995), we convolve the spectrum with the transmission filters and obtain the model fluxes to be compared with the observed ones. The best fit model is obtained by minimization of the merit function

$$\text{MF} = \sum_{i=1}^n \left( \frac{M_i - O_i}{E_i} \right)^2, \quad (5)$$

where  $M_i$ ,  $O_i$  and  $E_i$  are the model values, the observed values and the observational errors respectively, including the IR luminosity. The minimization is performed with an Adaptive Simulated Annealing algorithm (Ingber 1989).

We stress that the IR luminosity is a prior that provides the unbiased level of the SFR. For a given IMF, the error on the SFR is mainly observational, though there is some dependence on the adopted attenuation law and on the metallicity of the stellar populations, as already discussed by Shapley et al. (2005). Determining the correct shape of the SFR will require additional information, such as spectral emission, absorption lines and (non-)thermal radio continuum. These effects probe diverse contributions from stellar populations of different ages and can be used, in principle, to disentangle the correct shape of the SFR (e.g. Bressan et al. 2002; Vega et al. 2008).

With the SFR essentially determined by the IR luminosity, the observed  $UV$  continuum mainly sets the level of attenuation. This is also a quite robust result because the IR luminosity is mainly produced by the absorption of  $UV$  light. The observed SED from the  $UV$  to the near-IR results from the combination of the attenuation shape and the age of the galaxy. There can be some level of degeneracy between age, metallicity and attenuation shape, but the number of constraints is also quite large.

Finally, the stellar mass  $M_*$  is obtained by multiplying the SFR by the galaxy age  $t_g$  which amounts to the age of the oldest stellar population required by the fitting procedure.

## 5 RESULTS

In this Section we present and discuss our main findings.

### 5.1 Comparison between the Two Different Synthesis Methods

To begin with, we compare the results obtained with and without the use of the IR prior. We are reminded that in the latter case, which we name the standard procedure, we have also assumed a definite attenuation shape, i.e., a Calzetti law with  $R_V = 4.05$ .

Figure 2 (right panels) shows a few examples of best fit models obtained with the IR prior. The red crosses refer to the observed fluxes, while the triangles to the corresponding model fluxes (after convolution with the transmission filters). All the galaxies have also been fitted with the standard procedure and the best fit models are shown in Figure 2 (left panels). We see that even without the IR prior the best fit is in general fairly good, however the inferred star formation is different.

In Figure 3 we compare the SFR derived with and without the IR prior for the whole sample; symbols and color-codes are the same as in Figure 1 for ULIRGs, LIRGs and LLIRGs. Data with uncertainties  $\leq 15\%$  on the  $24 \mu\text{m}$  flux are surrounded by boxes. For almost all the ULIRGs the SFR obtained without the IR prior is underestimated, even by a large factor. On the other hand, LIRGs are distributed across the Meurer relation with quite a large dispersion. The latter decreases for the less luminous LLIRGs. Part of the dispersion is certainly due to our assumed value  $\text{IR}8 \approx 8.5$ , since less compact star-forming galaxies show a lower average value ( $\text{IR}8 \approx 5$ ) while more compact

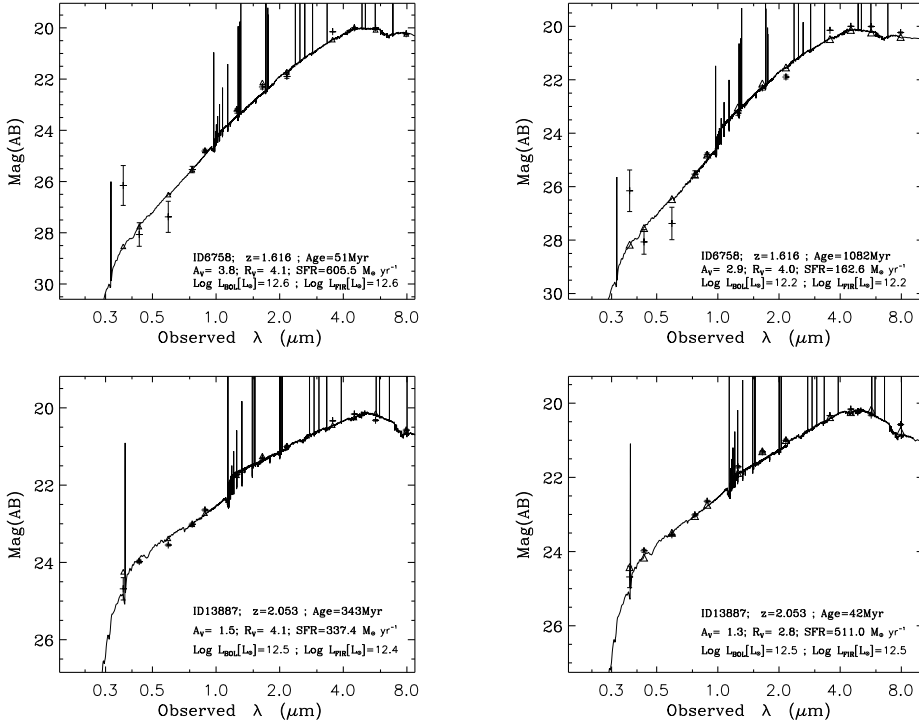


**Fig. 2** Best fit models obtained with (*right panels*) or without (*left panels*) the IR prior derived from the IR8 relation. In the former case the  $R_V$  parameter of the attenuation law is not fixed while in the latter case the value  $R_V = 4.05$  is adopted. The observed fluxes are plotted with crosses while corresponding model fluxes, after convolution with the transmission filters, are plotted with triangles. The solid curve is the best fit model. Both the SFR and the attenuation are kept constant with the age of the stellar populations. Error bars on fluxes are also plotted but are in general smaller than the size of the symbol.

star-forming objects show a higher average value ( $IR8 \approx 13$ ). Thus we could have overestimated the IR luminosity of the less compact galaxies and underestimated that of more compact objects, by about 50%, which translates into a similar scatter in the plot of Figure 2. However, the dispersion is actually significantly larger than this estimate, reaching in some cases a factor of five. Therefore it must be intrinsic to some extent.

The presence of galaxies for which the predicted SFR is underestimated is actually expected, because a significant fraction of the SFR could be entirely hidden due to strong attenuation. It has already been shown that in several local LIRGs and ULIRGs the SFR determined by the  $H\alpha$  or  $Pa\alpha$  luminosity, even corrected for attenuation with the Balmer decrement method, turn out to be lower by even a factor of three compared to what is obtained from the IR luminosity (see Poggianti et al. 2001; Valdés et al. 2005). On the other hand, the presence of objects for which the standard SED fitting technique overestimates the IR flux is a bit more intriguing. As a matter of fact, in these objects the reddening deduced from the  $UV$ /near-IR SED, if interpreted by means of the usual Calzetti law, would require a higher overall attenuation and this would produce an IR luminosity which is larger than the observed one. For the LLIRGs the use of a prior in the IR luminosity is not as important as for the higher luminosity galaxies. We will come back to this point at the end of the Section.

To proceed with the comparison between the two synthesis methods, in Figure 4 we show the galaxy ages and in Figure 5 the stellar masses. The latter mass is computed as the integral of the SFR over the galaxy age, and it does not take into account stellar recycling into the interstellar medium. We see that the age determination is, in general, quite independent of the IR prior. However, there is a minority of galaxies for which there is a large discrepancy between the two age determinations, with the ages determined with the IR prior turning out to be significantly larger than those based on the standard procedure. Furthermore, when the IR prior implies larger ages then it also implies lower SFRs, so that the differences in the masses obtained with the two methods are smoothed out. Nevertheless, it is also clear that the standard procedure underestimates the total mass by an average factor of about 50%, with some individual values that may be offset by even a factor of four.

For LLIRGs the masses derived using the two different methods are in fair agreement. In this class the attenuation is not strong enough to totally enshroud the star-forming regions and the SFR can be obtained directly from the fit of the  $UV$ /near-IR SED. Actually, the SFRs obtained with the standard procedure are even slightly overestimated for the majority of these sources. The reason behind this effect is that the standard procedure assumes the Calzetti law, whose  $R_V$  is larger than the characteristic value of low star-forming objects, as can be seen from Figure 1. In fact, the median value of  $R_V$  for objects in the LLIRG class is  $R_V \approx 3.0$ . Notice that, as shown in the following, the average age of these LLIRGs is about 0.9 Gyr, and thus their location in Figure 1 must be compared with the dashed line referring to a model with  $R_V = 3$  and an age of 1 Gyr. Once repeated with such a lower value of  $R_V$ , the results obtained with the standard procedure compare fairly well to those obtained with the IR prior.

This point is interesting because it allows us to increase the sample for which a robust estimate of the parameters can be obtained with the SED fitting technique. In particular, the number of LLIRGs is small and to draw more robust conclusions it would be desirable to extend the above analysis to the full  $z_{850}$ -selected sample. We are reminded that, in order to adopt the IR prior, we only use the sources detected at  $24 \mu\text{m}$ , with a detection threshold corresponding to an SFR of about  $10 M_\odot \text{yr}^{-1}$ . With this selection criterion we cut about half of our original  $z_{850}$ -selected sample, with the majority of the excluded objects belonging to the lower luminosity class. The experiment described above shows that we may release the constraint of the IR prior in the subsample of galaxies undetected at  $24 \mu\text{m}$  provided that, in the standard procedure, we adopt a Calzetti law with a lower value of  $R_V \approx 3.0$ .

We have thus repeated the standard procedure with a lower value of  $R_V$  for the  $24 \mu\text{m}$  undetected sources. The SED fits for these galaxies are not as good as those for the sample detected at  $24 \mu\text{m}$ . These galaxies are intrinsically less luminous and the photometric uncertainties are on average larger,

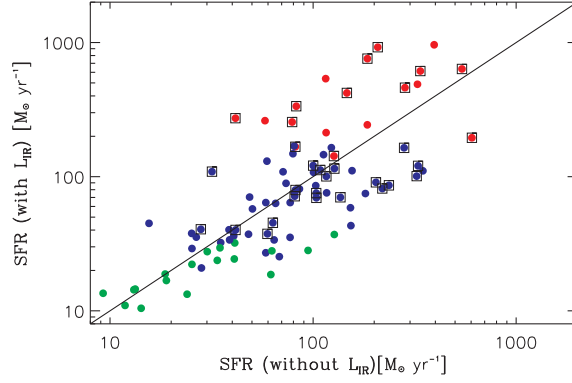


**Fig. 3** Comparison of the SED-inferred SFR obtained with and without the IR prior. The color code is the same as in Fig. 1; objects with error  $\leq 15\%$  on the 24  $\mu\text{m}$  flux have been surrounded by boxes.

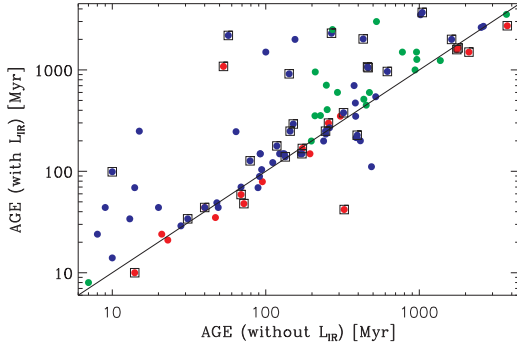


**Fig. 4** Same as Fig. 3 for the age.

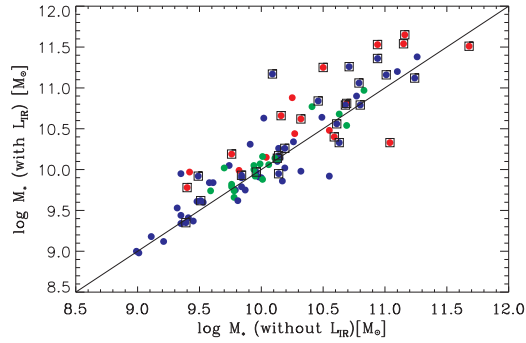


**Fig. 5** Same as Fig. 3 for the stellar masses.

typically being between 0.2–0.5 mag in about half of the bands. In several objects the derived SFR is higher than the average threshold imposed by the 24  $\mu\text{m}$  criterion, but the object was not detected at 24  $\mu\text{m}$  either because of a lower exposure depth or because the SED-inferred SFR was significantly affected by photometric errors. We thus excluded those objects from this sample with a derived SFR  $\geq 30 M_{\odot} \text{ yr}^{-1}$  for which, according to Figure 3, the knowledge of the IR prior is mandatory. After this further cut, we are left with 41 objects with  $L_{\text{IR}} \leq 10^{11} L_{\odot}$ . This subsample is constituted by the 24  $\mu\text{m}$  undetected galaxies for which the standard procedure allows a fairly robust estimate of the physical parameters. In the following we will also consider the galaxies of this subsample that we will refer to as 24  $\mu\text{m}$  undetected LLIRGs.

## 5.2 SFR and Attenuation

Figure 6 shows the distribution of the SFRs for our sample. The primary selection in the  $z_{850}$ -band allows us to detect galaxies with a wide range of SFRs, from a few to  $\geq 10^3 M_{\odot} \text{ yr}^{-1}$ . We recall from the above that in the SED fitting technique we have assumed  $R_V$  to be a free parameter. The upper left panel in Figure 7 shows the resulting values of  $R_V$  as a function of the SFR. We notice a broad tendency of  $R_V$  and the associated scatter to increase with the strength of the SFR. Part of the scatter could be due to the error accumulated in the process of obtaining the IR luminosity, whose largest contribution is given by the assumption of a single average relation with the 8  $\mu\text{m}$  luminosity IR8. However, a similar scatter is also evident in analogous plots for local sources, for which this

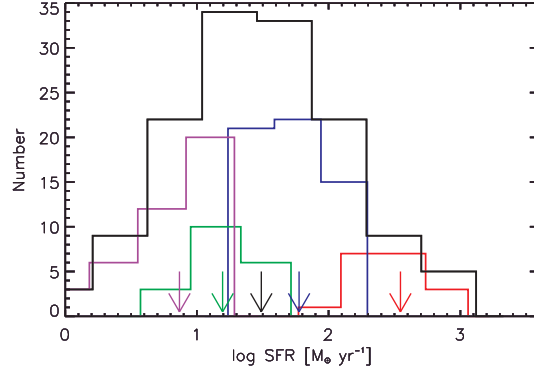


**Fig. 6** Distribution of the SFR in our galaxy sample. Histograms highlight the distributions and arrows mark their average values. The color code refers to the subsamples defined in Figure 1 (*red* for ULIRGs, *blue* for LIRGs and *green* for LLIRGs), to the 24  $\mu\text{m}$  undetected LLIRGs (*purple*) and to the overall sample (*black*).

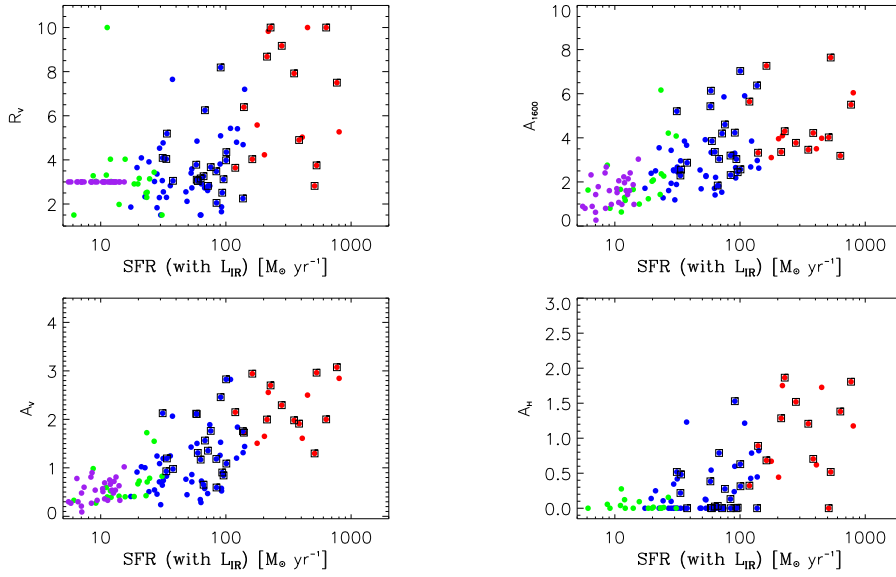


**Fig. 7** Dependence of the selective to global attenuation ( $R_V$ ), and of the attenuation in the UV ( $A_{1600}$ ), in the visual ( $A_V$ ) and in the  $H$ -band ( $A_H$ ) on the SFR. The color code is the same as in Fig. 6.

uncertainty is smaller, suggesting that there is an intrinsic dispersion connected with the shape of the attenuation law.

As already discussed in Section 3, at decreasing  $\beta_{UV}$  the loci with different  $R_V$  converge to a single curve. Therefore one would expect that the scatter in the inferred  $R_V$ , due to errors in either  $\beta_{UV}$  or  $L_{IR}$ , increases at decreasing  $\beta_{UV}$ . On the other hand, all LLIRGs with small  $\beta_{UV}$  exhibit a quite narrow scatter around  $R_V \approx 3$ . Note that the peculiar object represented by the green dot appearing in the upper left corner features a very high value  $R_V = 10$  and very old age 3 Gyr. It

has been retained in the sample because formally the  $\chi^2$  value of the SED fitting is low, but a visual inspection shows that the corresponding data suffer from large uncertainties.

To better stress the meaning of the  $R_V$  parameter, we are reminded that for the Calzetti law  $R_V \approx 4$  and that, by increasing  $R_V$ , the attenuation law becomes progressively flatter, i.e., more neutral. In particular, while for a typical Calzetti law the ratio of the attenuation in the  $K$  and  $V$  band is  $A_K/A_V \approx 0.1$ , for  $R_V = 10$  it increases to  $A_K/A_V \approx 0.6$ . Thus we expect that there will be a number of galaxies for which the attenuation in the near-IR band is not negligible with respect to that in the visual band, as usually assumed in star-forming galaxies. Indeed, several ULIRGs in our sample are well fitted by an attenuation law which is more neutral than the typical Calzetti law. In order to reproduce their observed IR luminosity together with the observed  $UV$  slope, a flat attenuation law is required, otherwise the predicted spectral slope would be too steep. This is consistent with the evidence that, in several local ULIRGs, the molecular clouds associated with the star-forming regions are optically thick even in the near-IR (Vega et al. 2008). In such galaxies the bulk of IR and  $UV$  luminosity could originate from different regions, as found in nearby starburst galaxies (Goldader et al. 2002). Thus the emerging  $UV$  radiation could not even directly mirror the global attenuation of the star-formation process, because the former may originate in regions that are occasionally located in a less dusty region of ambient space, or in a few regions where young stars emerge from the dusty ambient space on a relatively shorter timescale (Silva et al. 1998; Panuzzo et al. 2003). Our parametrization is meant to be a fair description of the attenuation resulting from the combination of all the intervening processes such as age-dependent extinction, geometrical effects and real differences in the dust mixture.

In the other panels of Figure 7 we show the relation between the SFR and the attenuation in the  $UV$  ( $A_{UV}$ ), in the optical ( $A_V$ ) and in the near-IR ( $A_H$ ). In all cases the attenuation grows with the SFR, as found by other authors, though the scatter is large. The scatter of the attenuation in the  $UV$  is not unexpected and is even consistent with the knotty nature of  $UV$  images. The distribution of the  $UV$  attenuation is shown in Figure 8. The median values for the different subclasses decrease at decreasing luminosity, while for the whole sample the median value is  $A_{UV} \approx 2.3$  mag and the maximum value is  $A_{UV} \approx 9$  mag. However, the distribution is clearly asymmetrical with a sharp drop above  $A_{UV} \approx 4$  mag. This could be related to the strong  $UV$  dimming suffered by galaxies with large  $A_{UV}$ . Indeed, two-thirds of the galaxies above the sharp drop are ULIRGs. As to the near-IR, we notice that the attenuation there may reach values that are significantly higher than those expected in the  $UV$  (or in the visual) by assuming a standard extinction law.

### 5.3 Stellar Masses and Ages

The distribution of stellar masses in our sample is shown in Figure 9. The masses range from  $M_* \approx 10^9 M_\odot$  to  $M_* \approx 4 \times 10^{11} M_\odot$ . ULIRGs have a quite flat mass distribution up to the higher values, and a median value of  $M_* \approx 4.2 \times 10^{10} M_\odot$ . By contrast, LIRGs and LLIRGs show more peaked distributions with median values of  $M_* \approx 9 \times 10^9 M_\odot$  and  $M_* \approx 2 \times 10^9 M_\odot$ , respectively. Notice that the median value for the LLIRGs detected in the mid-IR is significantly larger than the corresponding value for the LLIRGs that are not detected in mid-IR and is more similar to that of LIRGs,  $M_* \approx 1.1 \times 10^{10} M_\odot$ . This shows that the  $24 \mu\text{m}$  cut at low luminosity introduces a bias toward the more massive objects.

The age distribution of our galaxies is plotted in Figure 10. Notice that the definition we give here for age is different from that usually adopted when galaxy SEDs are analyzed by means of a unique SSP. In this latter case one derives the luminosity-weighted mean age of all the stellar populations present in the galaxy. In our case we refer to the age of the oldest population present in the galaxy. This is a free parameter in the fit that is only constrained by a maximum value, which is the Hubble time at the galaxy redshift. The lower limits for the ages of ULIRGs and LLIRGs are not significantly different and, perhaps more importantly, both classes contain very young objects, with

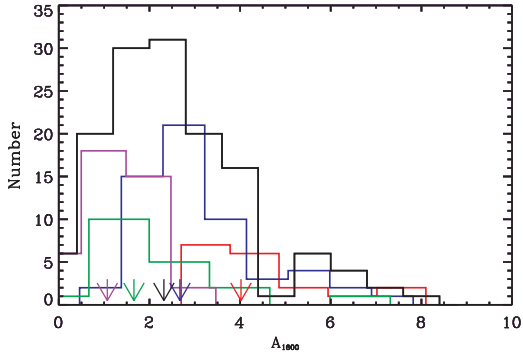


**Fig. 8** Distribution of the  $UV$  attenuation ( $A_{1600}$ ) in our galaxy sample. The color code is the same as in Fig. 6.

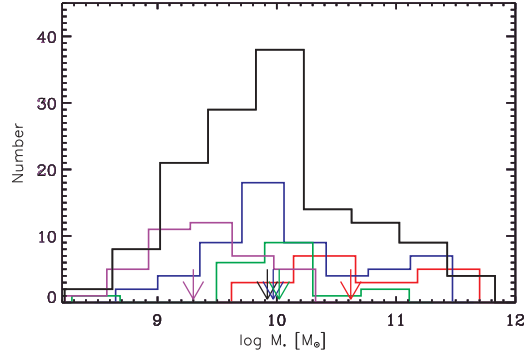


**Fig. 9** Distribution of the stellar masses in our galaxy sample. The color code is the same as in Fig. 6.

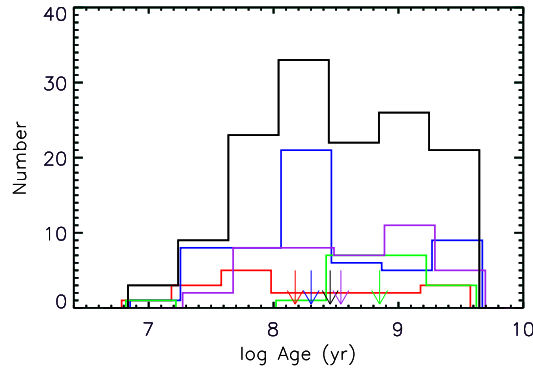


**Fig. 10** Age distribution of our galaxy sample. The color code is the same as in Fig. 6.

ages of only a few tens of Myr. This is particularly relevant for the ULIRGs because it is a strong and direct indication that a significant amount of dust must already be in place after such a short timescale.

The median age of the sub-samples increases with decreasing IR luminosity. For ULIRGs it is  $\approx 150$  Myr, for LIRGs it is  $\approx 200$  Myr and for LLIRGs it reaches  $\approx 900$  Myr. The latter value decreases to  $\approx 600$  Myr if we consider the LLIRGs that are undetected at  $24 \mu\text{m}$ . The distribution of ULIRGs is significantly flatter than that of LIRGs and in all cases objects as old as about 2 Gyr have been found. By contrast, the distribution of LIRGs and LLIRGs is skewed toward significantly older ages. Given the meaning of our age, this actually means that, on average, less luminous galaxies look older than more luminous ones. At first glance this evidence could appear to contradict the popular downsizing scenario, according to which less massive galaxies should be younger (e.g., Noeske et al. 2007; Clemens et al. 2010). We notice, however, that the downsizing scenario is generally based on luminosity-weighted ages that, as already stated, are averaged over all the stellar populations in a galaxy. Thus a likely possibility to reconcile both observational results is that the star formation in low luminosity galaxies started first but, having a lower efficiency or suffering less from impulsive energy feedback (likely from quasars), can be maintained for a longer time. Thus low mass objects would on average form first but they would appear younger nowadays because their star formation

lasted for a longer time. This interpretation would also be fully consistent with the evidence that the partition of heavy elements in local galaxies with lower luminosity is progressively less  $\alpha$ -enhanced (e.g., Clemens et al. 2010), another fact that can be explained by an increasing duration of the star formation process.

Yet another possibility to explain the above observation is that the duty cycle of the more massive objects is shorter both because of a shorter duration of star formation and of a rapid increase in the dust content that renders these objects undetectable in the  $UV$ /optical after a short timescale. In this case we will also preferentially observe younger objects. Despite this, relatively older massive galaxies could also be included in the current sample if their average attenuation decreases near the completion of their star formation history. In any case, our findings are consistent with the predictions of a downsizing scenario induced by an anti-hierarchical mass assembly process in which lower mass galaxies on average do form first, but their star formation lasts for a longer period due to their inability to get rid of the gaseous component (see Granato et al. 2004; Lapi et al. 2011). In the more massive objects, the quasar feedback is instead able to remove the gas fueling on a shorter timescale (see Lapi et al. 2006).

Figure 11 shows the specific star formation rate ( $sSFR=SFR/M_*$ ) as a function of the stellar mass  $M_*$ . We also plot the three loci with constant  $SFR = 10, 10^2$  and  $10^3 M_\odot \text{ yr}^{-1}$ , from left to right. In a similar figure, Reddy et al. (2006) showed that their galaxies lie in a narrow band, suggesting an eventual relation of the  $sSFR$  with the mass of the galaxy. However, their objects that were not detected by MIPS at  $24 \mu\text{m}$  occupy a lower region, indicating that the above hint may result from a bias induced by the adopted selection criteria. Our selection allows us to extend the range both at higher and at lower SFR, and we do not find any noticeable trend of the  $sSFR$  with the mass of the galaxy. Actually, the  $sSFR$  may change by about two orders of magnitude for masses up to  $M_* \approx 10^{11} M_\odot$ .

#### 5.4 Mass to Light Ratios

In Figure 12 we plot the intrinsic (i.e., the luminosity is corrected for attenuation) mass to light ratio in the rest-frame  $H$  band, in solar masses per solar  $H$ -band luminosity, vs. the absolute  $H$ -band magnitude. In the left panel we plot the results obtained with our procedure while in the right panel we show the results obtained by adopting the standard procedure for comparison. The mass to light ratios span a factor of  $\geq 30$  from 0.02 to 0.6 in both cases. The agreement is due to the fact that, for a constant SFR, the intrinsic  $M_*/L$  ratio is only a function of age and the age distribution is similar (though the age of individual objects is not exactly same).

However, we notice that in our case one cannot simply rely on the notion that the attenuation in the near-IR is low. Especially in the brightest galaxies, the attenuation in the near-IR may be large and neglecting this effect would produce a significantly higher  $M_*/L$  ratio. To better clarify this point in Figure 13 we plot the mass to light ratio versus the galaxy age. The data points correspond to the observed luminosity while the solid line represents the locus of the unattenuated models. We see that the intrinsic  $M_*/L$  ratios range from 0.02 to about 0.6 while, obviously, the uncorrected  $M_*/L$  ratio reaches much higher values. The observed spread at a given age is only due to attenuation.

Other authors claimed to have detected high  $M_*/L$  ratios in high redshift galaxies, even consistent, in the near-IR passbands, with those of local old metal-rich systems (see Shapley et al. 2005; Shapley 2011). Since they have used the standard procedure, where at these wavelengths the attenuation is negligible, we conclude that the difference with respect to our finding is simply due to the differences in the underlying stellar populations. As we already said, the  $M_*/L$  ratios in models with constant SFRs only depend on the age and thus these claims imply that, in the adopted models, the  $M_*/L$  ratios of intermediate age populations are similar to those of old systems. Thus for a constant SFR model it is impossible to reach, after a few of Gyr, the values of  $M_*/L \geq 1.5$  observed in local passively evolving spheroids.

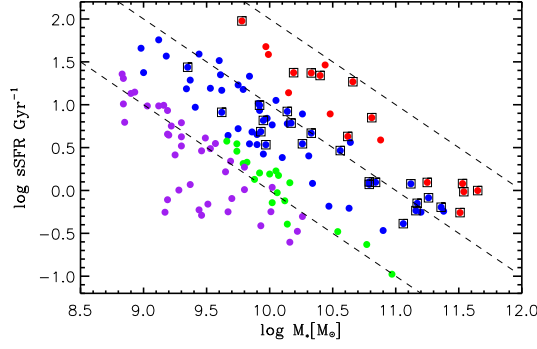


**Fig. 11** Specific star formation rate as a function of the stellar mass. The color code is the same as in Fig. 6. Dashed lines refer to a constant SFR of  $10$ ,  $10^2$  and  $10^3 M_{\odot} \text{ yr}^{-1}$  from left to right, respectively.

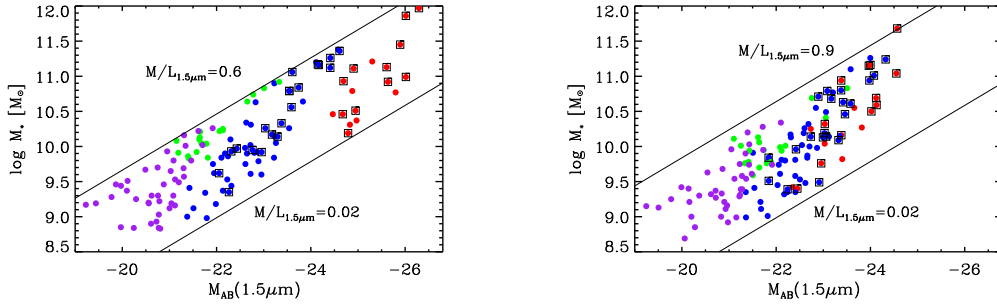


**Fig. 12** *Left Panel*: intrinsic mass to light ratio of our galaxies in the rest-frame  $H$ -band, in solar masses per solar  $H$ -band luminosity, vs. the absolute  $H$ -band magnitude. *Right panel*: the corresponding diagram obtained with the standard procedure. The color code is the same as in Fig. 6.

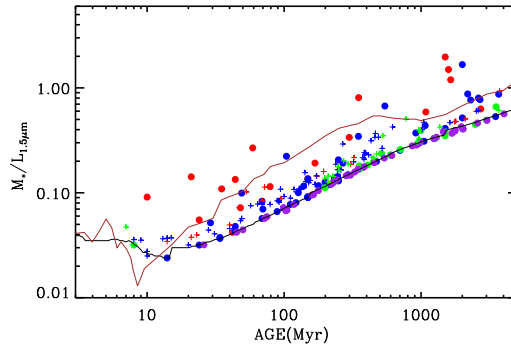


**Fig. 13** Observed mass to light ratio in the rest-frame  $H$ -band vs. the galaxy age. The color-code is the same as in Fig. 6. The luminosities are the observed ones, i.e., without dust correction. The circles represent the results according to our SED-fitting technique (IR prior and variable  $R_V$ ), while the crosses refer to the standard technique (no IR prior and  $R_V = 4.05$ ). The lines represent the locus of the unattenuated models, for a continuous SFR (*black*) and a unique SSP (*brown*).

## 6 SUMMARY

We have constructed a sample of 298 spectroscopically-confirmed galaxies at redshift  $z \sim 2$ , selected in the  $z_{850}$ -band from the GOODS-MUSIC catalog, with an SED well-sampled from the  $UV$  to the IR. This allows the analysis of the physical parameters of the galaxy by means of the popular SED-fitting technique. In doing this, we have adopted simple and standard assumptions like constant SFR, solar metallicity and age-independent attenuation.

The  $z_{850}$ -selection includes objects with a wide range of SFR, between a few to  $10^3 M_{\odot} \text{ yr}^{-1}$ , and with different strengths of the attenuation. Since about half of the sample (135 objects) has been detected at  $24 \mu\text{m}$  with *Spitzer* and since it has been claimed that the rest frame  $8 \mu\text{m}$  luminosity is quite a good proxy for the SFR, we have checked, for the first time in an intermediate redshift sample, the accuracy of the standard SED fitting technique.

We find that the standard SED fitting technique is not accurate enough to provide a reliable estimate of the SFR and, correspondingly the attenuation, the galaxy age or stellar masses.

There is a large scatter in the predicted vs. expected IR luminosity (that can even reach a factor of  $\approx 50$ ). The discrepancy increases at increasing star formation and, for the ULIRGs, the standard technique underestimates the SFR by even an order of magnitude. Surprisingly, the discrepancy is not limited to the most obscured galaxies, as expected, but it is also present in the low luminosity sample and, in some cases, the SED-inferred SFR is even larger than that probed from the observed  $24 \mu\text{m}$  luminosity. The total mass is on average underestimated by an average factor of about 50%, but individual values may be offset by even a factor of four.

Combining the observed IR luminosity with the observed  $UV$  spectral slope we have also constructed the rest frame IRX- $\beta_{UV}$  diagram for this redshift  $z \sim 2$  sample. This diagram is similar to other ones existing in literature and shows a large spread around the average Meurer relation. This spread can be well reproduced by changing the ratio between the neutral and the selective attenuation ( $R_V$ ) in the Calzetti law. We interpret this fact as an actual difference between extinction and attenuation laws, with the latter being the result of a combination of many effects, such as an age-dependent extinction, complex geometries of dust and stars, and possible differences between grain compositions and sizes.

We have thus reanalyzed the subsample detected at  $24 \mu\text{m}$  by exploiting the constraint imposed by the total IR luminosity and the possibility of varying the attenuation law. Moreover, instead of adopting usual conversions from the IR to the SFR (see Kennicutt 1998; Panuzzo et al. 2003), that only hold in particular conditions (e.g., fixed duration of the star formation episode, given geometry, etc.) we have used the observed IR luminosity as a constraint in the SED-fitting technique.

As a result we have outlined a new method that should be used when the knowledge of the IR luminosity can be added to the global SED. The most noticeable difference between the methodology used in the present work compared with previous works rests on:

- (1) The use of the IR constraint, here derived from the observed  $24 \mu\text{m}$  luminosity;
- (2) The use of a generalized Calzetti law with a variable  $R_V$ .

With this new method we have determined in an unprecedented robust way the physical parameters that characterize our galaxies, namely SFR, attenuation and age.

- **Attenuation.** There is a general trend of increasing attenuation with SFR, or, equivalently, with the unobscured absolute  $UV$  magnitude, but the correlation is not tight. The ratio  $R_V$  shows a large scatter at all values of the SFR indicating a variety of concomitant effects that may have a bearing on the combined attenuation law. This was already suggested by our IRX- $\beta_{UV}$  diagram but the trend in the scatter with the SFR is more indicative that these processes appear at any scale.

The relation between the attenuation and the SFR becomes tighter toward larger wavelengths. This is consistent with the fact that in general at shorter wavelengths images show more knotty structures that combine overall to give a different attenuation curve. High values of  $R_V$  are generally required to fit the SEDs of ULIRGs. In this case the attenuation curve is very flat and the attenuation remains relatively significant even in the near-IR. Indeed, from the analysis of local ULIRGs, it was expected that a fraction of the star formation could be significantly attenuated even at these long wavelengths. For the low luminosity galaxies a knowledge of the IR prior is not as important as for those with high luminosity. This threshold corresponds to an SFR of about  $20 M_\odot \text{ yr}^{-1}$ . However, if we use a pure Calzetti law for these galaxies, the standard procedure slightly overestimates the SFR. A more suitable attenuation law is that with  $R_V \approx 3.0$ . There is a fair relation between the  $UV$  attenuation and the  $z_{850} - 4.5 \mu\text{m}$  color. This could eventually be used to obtain the absolute  $UV$  magnitude in the absence of an IR luminosity prior, but its effective usefulness has not been studied in detail, and is deferred to a future work.

- **Star formation rates, ages and masses.** Our  $z_{850}$ -selected sample includes objects with a wide range of SFRs, between a few to  $10^3 M_\odot \text{ yr}^{-1}$ . The average SFR is about  $80 M_\odot \text{ yr}^{-1}$ . In this respect the sample complements other ones selected by means of the drop-out technique.

The mass distribution ranges from  $10^9$  to  $4 \times 10^{11} M_\odot$ . If we take into account the sample of low luminosity sources that are not detected at  $24 \mu\text{m}$ , there is strong evidence that the average mass increases at increasing star formation. ULIRGs show a flat mass distribution with a minimum mass of  $1.2 \times 10^{10} M_\odot$ .

The age distribution of our sample ranges from a few tens of Myr to more than 1 Gyr. For the first time we have obtained accurate ages of severely obscured, intermediate redshift objects with very high SFRs. Individual age measurements of highly attenuated objects indicate that dust must form within a few tens of Myr and already be copious by the time the most massive asymptotic giant branch (AGB) stars have evolved, i.e., at times  $\leq 100$  Myr. Low luminosity, star-forming galaxies detected at  $24 \mu\text{m}$  show on average a significantly more prolonged star formation with respect to more luminous star-forming objects, though their mass is not significantly different. However, the  $24 \mu\text{m}$  detection threshold is too high for this subsample and must be reduced in order to produce a statistically significant number of objects. By releasing this constraint and using the attenuation law with  $R_V \approx 3.0$  in the standard procedure, we could increase the subsample to 41 galaxies. As explained above, for low luminosity objects this method does not affect the accuracy of the results.

With this increased sample we confirm that low luminosity galaxies harbor, on average, significantly older stellar populations and are also less massive than the brighter ones. Those selected at  $24 \mu\text{m}$  actually constitute the brightest tail of the low-luminosity subsample. Thus we confirm that the observed downsizing effect (lower mass galaxies appearing younger) is consistent with a picture where less massive galaxies actually form first, but their star formation lasts longer, consistent with an anti-hierarchical galaxy formation scenario.

- **Specific star formation rate.** We do not find any trend of the sSFR with the mass of the galaxy as claimed by other authors. We discuss how the previously observed trend can be spurious and results from a bias induced by the selection criteria of the analyzed samples.
- **Mass to light ratios.** We find that care must be taken when dealing with  $M_*/L$  ratios because, while it is customarily assumed that attenuation is scarce at near-IR wavelengths, one remarkable result of our investigation is that this is not the case for luminous objects. After imposing the IR constraint we find that, in order to fit the whole SED, we need a flatter attenuation curve. This implies that the attenuation is not negligible at near-IR wavelengths. Correspondingly, the near-IR  $M_*/L$  ratios obtained after a proper attenuation correction never reach those of nearby galaxies, as claimed by other authors, and remain lower by about a factor of three. In this respect

the objects with the higher  $M_*/L$  ratio are the low luminosity sources, because they are also the oldest galaxies.

**Acknowledgements** This work has been supported by the National Natural Science Foundation of China (Grant No. 11203023) and Chinese Universities Scientific Fund (WK 2030220011, WK 2030220004 and WJ 2030220007). L.F. thanks the partial financial support from the China Postdoctoral Science Foundation (Grant Nos. 2012M511411 and 2013T60615). A.L. thanks the partial support by ASI and MIUR.

## Appendix A: SIMPLE STELLAR POPULATION MODELS

The SSP models adopted here are computed following Bressan et al. (1998) but with the new empirical stellar spectral library MILES (Sánchez-Blázquez et al. 2006), which covers the parameter space of metallicity, effective temperature and gravity well and thus ensures good optical broadband starting colors. To cope with limitations in its spectral range we have extended the stellar spectra of MILES by means of matched NEXTGEN (Allard et al. 2000) models both in the far-UV and in the near-IR/mid-IR spectral region. For temperatures above 10 000 K we do not have NEXTGEN models and we have used the library by Munari et al. (2005) with the extension of the Lejeune models below 2500 Å and above 10 000 Å. In this way we have obtained three core libraries with average  $[M/H] = -0.5, 0.0$  and  $+0.3$ . The stellar spectra extend from 10 Å to 160 μm and the spectral resolution is about 2 Å FWHM, from 2500 Å to 10 000 Å. To take into account the effects of mass loss in hot supergiant stars we have considered two further extensions. For O stars we have considered the spectral models by Schaerer & de Koter (1997) while for Wolf-Rayet stars we have included the spectral models by Schmutz et al. (1992). The latter library only provides the continuum distribution of Wolf-Rayet stars but there are more recent stellar libraries that also provide spectral features (e.g., Smith et al. 2002). However, the Schmutz et al. library is suitable for our purposes because here we only consider broadband magnitudes and, more importantly, because its parametrization as a function of core temperature  $T^*$  and transformed radius  $R_t$  allows a fair interpolation between stellar evolution quantities ( $L$  and  $T_{\text{eff}}$ ) and spectral models of thick winds.

For the young populations we have also considered the nebular spectrum, which is calculated by means of CLOUDY (Ferland 1996) assuming case B recombination. To compute the nebular emission at different ages we have considered the corresponding spectra of the SSPs using the following parameters: mass of the ionizing cluster  $10^5 M_\odot$ , electron number density  $n = 100 \text{ cm}^{-3}$ , inner radius 15 pc, and the metallicity rescaled to that of the SSP. The nebular emission has then been suitably rescaled to the original mass of the SSP. The main effect we noticed on broadband fluxes is the contribution of nebular continuum in very young stellar populations. Changing the nebular parameters would not significantly affect our conclusions.

For intermediate-age stellar populations we have also considered the effects of dusty envelopes around AGB stars, as described in Bressan et al. (1998), but after revisiting the mass loss rate formulation and the expected dust composition, as described in Marigo et al. (2008). We have finally checked that the isochrones reproduce the observed integrated ( $V - K$ ) colors of star clusters of the Large Magellanic Cloud well (Persson et al. 1983; Kyeong et al. 2003; Pessev et al. 2006), especially at intermediate ages.

## References

- Adelberger, K. L., & Steidel, C. C. 2000, *ApJ*, 544, 218  
 Allard, F., Hauschildt, P. H., & Schweitzer, A. 2000, *ApJ*, 539, 366  
 Balestra, I., Mainieri, V., Popesso, P., et al. 2010, *A&A*, 512, A12

- Bavouzet, N., Dole, H., Le Floch, E., et al. 2008, *A&A*, 479, 83
- Bell, E. F. 2002, *ApJ*, 577, 150
- Boissier, S., Gil de Paz, A., Boselli, A., et al. 2007, *ApJS*, 173, 524
- Boselli, A., Lequeux, J., Sauvage, M., et al. 1998, *A&A*, 335, 53
- Bressan, A., Granato, G. L., & Silva, L. 1998, *A&A*, 332, 135
- Bressan, A., Silva, L., & Granato, G. L. 2002, *A&A*, 392, 377
- Buat, V., Iglesias-Páramo, J., Seibert, M., et al. 2005, *ApJ*, 619, L51
- Burgarella, D., Buat, V., & Iglesias-Páramo, J. 2005, *MNRAS*, 360, 1413
- Calzetti, D., Kinney, A. L., & Storchi-Bergmann, T. 1994, *ApJ*, 429, 582
- Calzetti, D., Armus, L., Bohlin, R. C., et al. 2000, *ApJ*, 533, 682
- Calzetti, D., Kennicutt, R. C., Jr., Bianchi, L., et al. 2005, *ApJ*, 633, 871
- Caputi, K. I., Lagache, G., Yan, L., et al. 2007, *ApJ*, 660, 97
- Cazaux, S., & Tielens, A. G. G. M. 2002, *ApJ*, 575, L29
- Cazaux, S., & Tielens, A. G. G. M. 2004, *ApJ*, 604, 222
- Chabrier, G. 2003, *PASP*, 115, 763
- Chapman, S. C., Blain, A. W., Smail, I., & Ivison, R. J. 2005, *ApJ*, 622, 772
- Chary, R., & Elbaz, D. 2001, *ApJ*, 556, 562
- Clemens, M. S., Jones, A. P., Bressan, A., et al. 2010, *A&A*, 518, L50
- Cortese, L., Boselli, A., Buat, V., et al. 2006, *ApJ*, 637, 242
- Caputi, K. I., Lagache, G., Yan, L., et al. 2007, *ApJ*, 660, 97
- Daddi, E., Cimatti, A., Renzini, A., et al. 2004, *ApJ*, 600, L127
- Dale, D. A., Silbermann, N. A., Helou, G., et al. 2000, *AJ*, 120, 583
- de Santis, C., Grazian, A., Fontana, A., & Santini, P. 2007, *New Astron.*, 12, 271
- Dickinson, M., Papovich, C., Ferguson, H. C., & Budavári, T. 2003, *ApJ*, 587, 25
- Draine, B. T. 2003, *ARA&A*, 41, 241
- Dwek, E. 1998, *ApJ*, 501, 643
- Elbaz, D., Dickinson, M., Hwang, H. S., et al. 2011, *A&A*, 533, A119
- Fan, L., Lapi, A., De Zotti, G., & Danese, L. 2008, *ApJ*, 689, L101
- Fan, L., Lapi, A., Bressan, A., et al. 2010, *ApJ*, 718, 1460
- Ferland, G. J. 1996, University of Kentucky Internal Report, 565 pages, <http://www.nublado.org/>
- Fontana, A., Donnarumma, I., Vanzella, E., et al. 2003, *ApJ*, 594, L9
- Förster Schreiber, N. M., Sauvage, M., Charmandaris, V., et al. 2003, *A&A*, 399, 833
- Förster Schreiber, N. M., van Dokkum, P. G., Franx, M., et al. 2004, *ApJ*, 616, 40
- Gil de Paz, A., Boissier, S., Madore, B. F., et al. 2007, *ApJS*, 173, 185
- Goldader, J. D., Meurer, G., Heckman, T. M., et al. 2002, *ApJ*, 568, 651
- Granato, G. L., De Zotti, G., Silva, L., Bressan, A., & Danese, L. 2004, *ApJ*, 600, 580
- Grazian, A., Fontana, A., de Santis, C., et al. 2006, *A&A*, 449, 951
- Helou, G., Lu, N. Y., Werner, M. W., Malhotra, S., & Silbermann, N. 2000, *ApJ*, 532, L21
- Hirashita, H., & Ferrara, A. 2002, *MNRAS*, 337, 921
- Ingber, L. 1989, *Mathematical and Computer Modelling*, 12, 967
- Kennicutt, R. C., Jr. 1998, *ARA&A*, 36, 189
- Kroupa, P. 2001, *MNRAS*, 322, 231
- Kyeong, J.-M., Tseng, M.-J., & Byun, Y.-I. 2003, *A&A*, 409, 479
- Labbé, I., Huang, J., Franx, M., et al. 2005, *ApJ*, 624, L81
- Lapi, A., Shankar, F., Mao, J., et al. 2006, *ApJ*, 650, 42
- Lapi, A., González-Nuevo, J., Fan, L., et al. 2011, *ApJ*, 742, 24
- Madau, P. 1995, *ApJ*, 441, 18
- Marigo, P., Girardi, L., Bressan, A., et al. 2008, *A&A*, 482, 883

- Meurer, G. R., Heckman, T. M., & Calzetti, D. 1999, *ApJ*, 521, 64
- Morgan, H. L., & Edmunds, M. G. 2003, *MNRAS*, 343, 427
- Munari, U., Sordo, R., Castelli, F., & Zwitter, T. 2005, *A&A*, 442, 1127
- Noeske, K. G., Weiner, B. J., Faber, S. M., et al. 2007, *ApJ*, 660, L43
- Nordon, R., Lutz, D., Shao, L., et al. 2010, *A&A*, 518, L24
- Nordon, R., Lutz, D., Genzel, R., et al. 2012, *ApJ*, 745, 182
- Ouchi, M., Shimasaku, K., Okamura, S., et al. 2004, *ApJ*, 611, 660
- Panuzzo, P., Bressan, A., Granato, G. L., Silva, L., & Danese, L. 2003, *A&A*, 409, 99
- Papovich, C., Dickinson, M., & Ferguson, H. C. 2001, *ApJ*, 559, 620
- Papovich, C., Dole, H., Egami, E., et al. 2004, *ApJS*, 154, 70
- Papovich, C., Moustakas, L. A., Dickinson, M., et al. 2006, *ApJ*, 640, 92
- Pérez-González, P. G., Rieke, G. H., Villar, V., et al. 2008, *ApJ*, 675, 234
- Persson, S. E., Aaronson, M., Cohen, J. G., Frogel, J. A., & Matthews, K. 1983, *ApJ*, 266, 105
- Pessev, P. M., Goudfrooij, P., Puzia, T. H., & Chandar, R. 2006, *AJ*, 132, 781
- Pettini, M., Kellogg, M., Steidel, C. C., et al. 1998, *ApJ*, 508, 539
- Poggianti, B. M., Bressan, A., & Franceschini, A. 2001, *ApJ*, 550, 195
- Poggianti, B. M., & Wu, H. 2000, *ApJ*, 529, 157
- Popesso, P., Dickinson, M., Nonino, M., et al. 2009, *A&A*, 494, 443
- Reddy, N. A., Steidel, C. C., Fadda, D., et al. 2006, *ApJ*, 644, 792
- Reddy, N. A., Erb, D. K., Pettini, M., Steidel, C. C., & Shapley, A. E. 2010, *ApJ*, 712, 1070
- Reddy, N. A., Pettini, M., Steidel, C. C., et al. 2012a, *ApJ*, 754, 25
- Reddy, N., Dickinson, M., Elbaz, D., et al. 2012b, *ApJ*, 744, 154
- Rieke, G. H., Alonso-Herrero, A., Weiner, B. J., et al. 2009, *ApJ*, 692, 556
- Rigby, J. R., Marcellac, D., Egami, E., et al. 2008, *ApJ*, 675, 262
- Rigopoulou, D., Franceschini, A., Aussel, H., et al. 2000, *ApJ*, 537, L85
- Salpeter, E. E. 1955, *ApJ*, 121, 161
- Sánchez-Blázquez, P., Peletier, R. F., Jiménez-Vicente, J., et al. 2006, *MNRAS*, 371, 703
- Santini, P., Fontana, A., Grazian, A., et al. 2009, *VizieR Online Data Catalog*, 350, 40751
- Sawicki, M., & Yee, H. K. C. 1998, *AJ*, 115, 1329
- Schaerer, D., & de Koter, A. 1997, *A&A*, 322, 598
- Schmutz, W., Leitherer, C., & Gruenwald, R. 1992, *PASP*, 104, 1164
- Seibert, M., Martin, D. C., Heckman, T. M., et al. 2005, *ApJ*, 619, L55
- Shapley, A. E. 2011, *ARA&A*, 49, 525
- Shapley, A. E., Steidel, C. C., Adelberger, K. L., et al. 2001, *ApJ*, 562, 95
- Shapley, A. E., Erb, D. K., Pettini, M., Steidel, C. C., & Adelberger, K. L. 2004, *ApJ*, 612, 108
- Shapley, A. E., Steidel, C. C., Erb, D. K., et al. 2005, *ApJ*, 626, 698
- Silva, L., Granato, G. L., Bressan, A., & Danese, L. 1998, *ApJ*, 509, 103
- Smith, L. J., Norris, R. P. F., & Crowther, P. A. 2002, *MNRAS*, 337, 1309
- Valdés, J. R., Berta, S., Bressan, A., et al. 2005, *A&A*, 434, 149
- Vanzella, E., Cristiani, S., Dickinson, M., et al. 2006, *A&A*, 454, 423
- Vanzella, E., Cristiani, S., Dickinson, M., et al. 2008, *A&A*, 478, 83
- Vega, O., Clemens, M. S., Bressan, A., et al. 2008, *A&A*, 484, 631
- Vijh, U. P., Witt, A. N., & Gordon, K. D. 2003, *ApJ*, 587, 533
- Witt, A. N., & Gordon, K. D. 2000, *ApJ*, 528, 799